Available online at www.sciencedirect.com

ScienceDirect

Procedia Manufacturing 34 (2019) 305–315

Procedia MANUFACTURING

www.elsevier.com/locate/procedia

47th SME North American Manufacturing Research Conference, Penn State Behrend Erie, Pennsylvania, 2019

Scanning and modeling for non-standard edge geometry endmills

Timothy No[a], Michael Gomez[a], Ryan Copenhaver[a], Juan Uribe Perez[b], Christopher Tyler[c], and Tony L. Schmitz*[a]

[a]*University of North Carolina at Charlotte, Mechanical Engineering and Engineering Science, Charlotte, NC, 28223, USA*
[b]*GOM Americas Inc., Charlotte, NC, 28223, USA*
[c]*The Boeing Company, Berkeley, MO, 63134, USA*

* Corresponding author. Tel.: +1-704-687-5086; fax: +1-704-687-8345. *E-mail address:* tony.schmitz@uncc.edu

Abstract

This paper describes a reverse engineering solution for modeling the behavior of non-standard edge geometry endmills. Structured light scanning is used to produce a solid model of the endmill and spatial coordinates for the points that define the cutting edges are extracted. These points are used to determine the cutting edge radius and angle at equally spaced points along the tool's axis. This cutting edge geometry is then incorporated in a time domain simulation that predicts cutting force and tool/workpiece deflection for user-selected operating parameters. Good agreement between predicted and measured cutting forces is first demonstrated. Second, the results of stability tests are compared to simulation predictions for multiple spindle speed-axial depth of cut combinations. The time records are analyzed by periodically sampling the measured and predicted displacement and velocity.

Keywords: Milling; dynamics; fringe projection; serrated; time domain simulation

1. Introduction

Multi-axis machining is a cornerstone manufacturing capability for discrete part production. Technology improvements are consistently pursued and implemented to increase productivity and efficiency. Examples include:

- new machine designs to increase part access, work volume, acceleration, velocity, stiffness, and accuracy
- controller improvements to reduce positioning and contouring errors
- new spindle designs to increase power, torque, rotation speed, and thermal stability
- new tool holder designs to increase clamping stiffness and reduce runout
- new tool designs to increase stiffness, provide localized cooling/lubrication at the tool/chip interface, segment chips, and increase material removal rates.

For endmills, design modifications to the cutting teeth include non-uniform spacing, variable helix angle, edge honing, and serrated edge geometry, among others. The purpose of these design updates are to affect chip formation and disturb the tooth-to-tooth chip thickness regeneration that serves as the mechanism for self-excited vibration, or chatter, in endmilling operations. While modeling of machining operations has received continuous international attention since the mid-20th century [1-3], relatively less effort has been expended on modeling the behavior of these non-standard geometry endmills, particularly those with serrated cutting edges. Notable exceptions include the following. Wang and Yang [4] presented force models in the angle and frequency domains for a cylindrical roughing end mill with sinusoidal cutting edges. Merdol and Altintas [5] modeled the serration profile by fitting points along a cubic spline projected on the helical flutes. This geometric model was used to generate a time domain milling model. Dombovari *et al.* [6] used the semi-discretization

2351-9789
10.1016/j.promfg.2019.06.154

method to analyze the stability of serrated end mills. Later, he and others created general models for various tool geometries [7, 8]. Koca and Budak [9] used a linear edge-force model and the semi-discretization method for force and stability modeling and optimized the serration waveform shape to reduce milling forces and increase stability. Grabowski *et al.* [10] extended their mechanistic model to calculate the process forces of serrated endmills. Tehranizadeh and Budak [11] proposed a genetic algorithm to optimize the design of serration shapes. While it is understood from these efforts that increased stable axial depths of cut are made possible by commercially-available edge geometries, modeling solutions for predicting forces, deflections, and stability are not widely available to industry.

In this paper, a complete solution for modeling the behavior of non-standard edge geometry endmills is provided. The procedure includes: 1) structured light scanning to produce a solid model of the endmill; 2) identification of the spatial coordinates for the points that define the cutting edges; 3) analysis of those points to extract the cutting edge radius and angle at equally spaced slices along the tool axis; 4) time domain simulation of the cutting force and tool/workpiece deflection using the measured edge geometry; and 5) periodic sampling of the simulation outputs to analyze stability.

The paper outline follows. In section 2, the structured light scanning approach is described and example results are presented. In section 3, the time domain simulation is detailed. In section 4, the experimental setup for milling trials is detailed. In section 5, a comparison of measured and simulated forces is presented for stable cutting conditions over a range of axial depths and feed per tooth values. The results of stability testing and predictions are also provided. Finally, conclusions are reported in section 6.

Fig. 1. Tool preparation for structured light scanning. (Left) example tool. (Right) application of *i*-PrOH TiO_2 coating and reference targets.

2. Scanning metrology for edge geometry

A primary challenge associated with modeling the performance of non-standard edge geometry endmills is that the design details are not generally available. To overcome this obstacle, the reverse engineering capabilities made possible by scanning metrology can be leveraged. One strategy for collecting point clouds from complex surfaces to develop the corresponding solid model is structured light, or fringe, projection. In this technique, a common approach is to project a pattern of parallel lines onto the surface in question. The reflected lines are distorted due to the surface geometry. The measurement system uses the relative positions of the projector and one or more cameras (two cameras is typical) together with the distorted lines to reconstruct the three-dimensional surface. While many commercial options are available, the GOM ATOS Capsule system was used for this research.

Fig. 2. Scanning metrology setup using the GOM ATOS Capsule system.

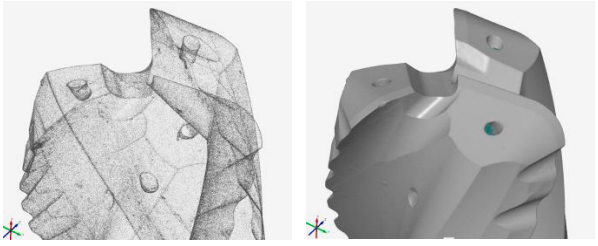

Fig. 3. Point cloud (left) and model (right) obtained from scanning.

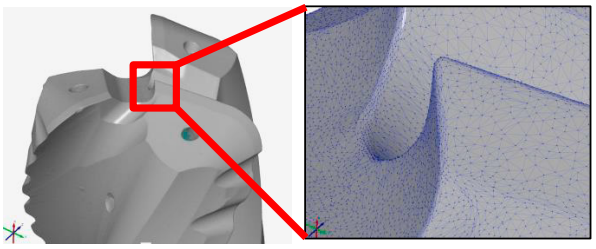

Fig. 4. Model (left) and mesh details (right) for endmill.

The measurements proceeded by first preparing the endmill surface using a removable anti-glare coating and attaching reference targets to the shank surface to enable multiple measurements to be stitched together and generate the solid model; a photograph is provided in Fig. 1. Multiple scans were then completed (Fig. 2) to obtain the point cloud and 3D model

(Fig. 3). Mesh details are provided in Fig. 4. Figures 2-4 display results for the focus tool of this study (Walter Tools, part number 3D1163-6768616).

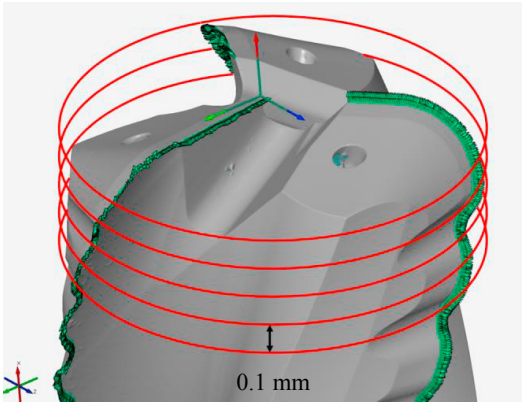

Fig. 5. Cutting edge points and axial slices (not to scale) for linear interpolation. The origin is also identified.

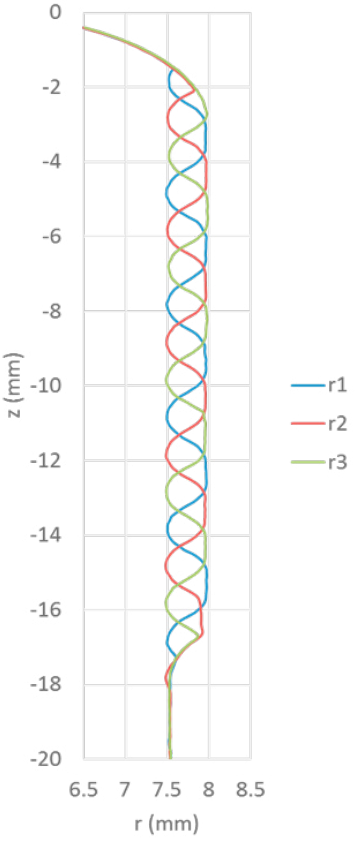

Fig. 6. Radius value at each axial slice for all three endmill teeth.

The procedure used to extract the edge coordinates from the solid model included four steps.

- First, using the best fit cylinder to the tool shank and the fluted end's extreme point, the origin was established on the tool's center line.
- Second, the points located on the cutting edges were selected. This step required manual manipulation within the GOM software. It was analogous to updating driving directions in Google Maps by dragging the original route to new roads.
- Third, the radius, r, and angle, ϕ, for each edge point was calculated. The teeth angles were normalized to a selected tooth and constrained to values between 0 and 360 deg; the z value was retained to obtain a triplet, $\{r, \phi, z\}$ for each point.
- Fourth, because the point density was higher than required for the time domain simulation, linear interpolation was used to obtain the triplet for axial slices located every 0.1 mm over the full flute length; see Fig. 5, which shows the origin, edge points, and axial slices.

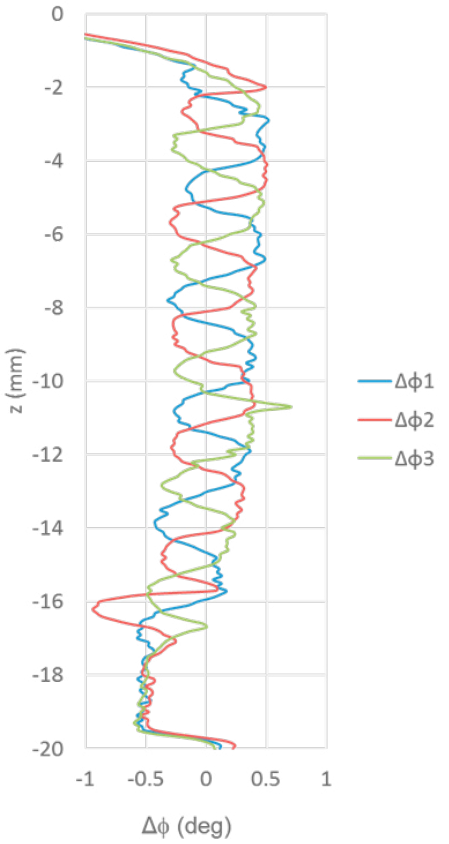

Fig. 7. Deviations of teeth angles from nominal helix.

Example radius and angle results are provided in Figs. 6 and 7. It is observed in Fig. 6 that the specialized tool geometry incorporates large radius variation along the cutting edge and that these radius variations are phased from one tooth to the next (120 deg spacing between the peaks for the three teeth). In Fig. 7, it is seen that the angle variation from the nominal helix, $\Delta\phi$, is not significant. The mechanism for increased stability with this design is, therefore, the segmentation of the cutting edge into bands using the radius variation. This effectively reduces the axial depth of cut, while simultaneously increasing the chip thickness. Also, the point cloud data was used to determine the

macro-geometry: 8 mm shank radius, 28.3 deg helix, and 2.785 mm bull nose radius.

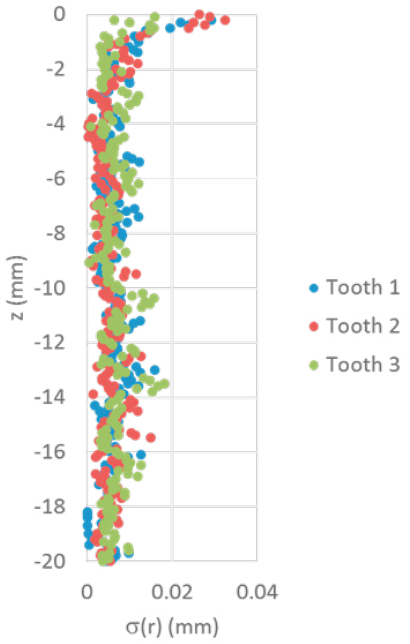

Fig. 8. Standard deviations in the radius, $\sigma(r)$, from the manual edge identification step.

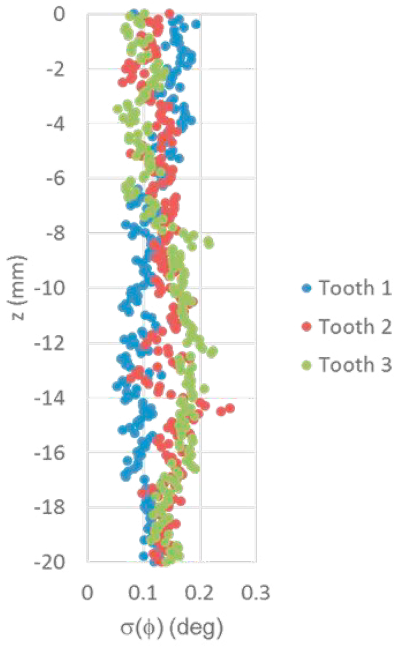

Fig. 9. Standard deviations in the teeth angles, $\sigma(\phi)$, from the manual edge identification step.

Due to the manual manipulation in the second step, it was desired to determine the sensitivity of the cutting edge coordinate identification and, by extension, the radius and angle values used in the time domain simulation. To assess this sensitivity, the manual manipulation used to identify the cutting edges was performed five times for each edge (15 total data sets) for a single measurement. This isolated the contribution of the edge identification from potential non-repeatability in the measurement (this uncertainty was not evaluated in this study). The standard deviations in the radius, $\sigma(r)$, and angle, $\sigma(\phi)$, are displayed in Figs. 8 and 9. It is seen that the deviations are small and the data is therefore sufficient to make meaningful process performance predictions when incorporated in the time domain simulation.

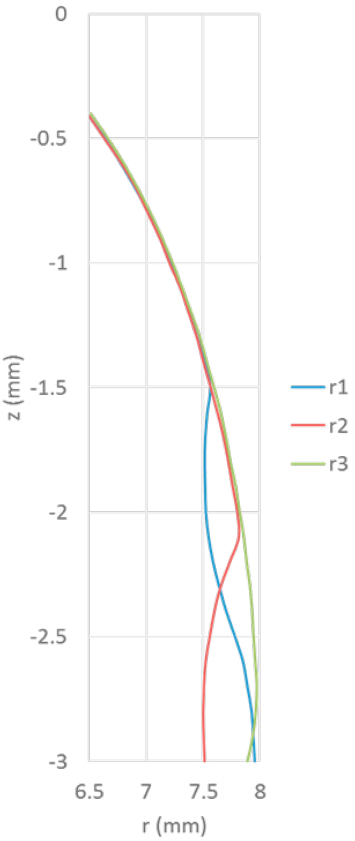

Fig. 10. Selection of tooth 3 as the reference tooth shape.

3. Time domain simulation

Time domain simulation enables numerical solution of the coupled, time-delay equations of motion for milling in small time steps [1]. It is well suited to incorporating the inherent complexities of milling dynamics, including the nonlinearity that occurs if the tooth leaves the cut due to large amplitude vibrations and complicated tool geometries (runout, or different radii, of the cutter teeth, non-uniform teeth spacing, and variable helix). The simulation applied here is based on the regenerative force, dynamic deflection model described by Smith and Tlusty [12]. As opposed to analytical stability maps that provide a global picture of the stability behavior, time domain simulation provides information regarding the local cutting force and vibration behavior for the selected cutting

conditions. The simulation used in this study is described in the following paragraphs.

The strategy used to model the large radius variation for each tooth (Fig. 6) was to define a nominal tooth shape with no serration and then incorporate the radial deviation as runout. It is observed in Fig. 10 that tooth 3 follows the nominal bull nose profile up to the shank diameter. The tooth 3 geometry was therefore selected as the reference up to -2.4 mm. The radius was then set to a constant value of 7.974 mm (i.e., the value at -2.4 mm) for z values of -2.5 mm and beyond. The runout was determined for each tooth as the difference between the reference profile and the actual radius value at each z interval. The runout, RO, is displayed in Fig. 11. The peak-to-peak variation is approximately 0.48 mm.

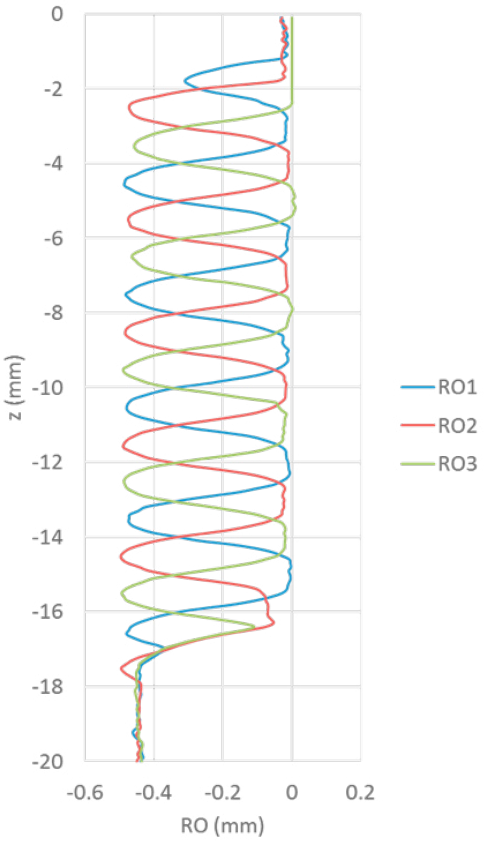

Fig. 11. Runout, RO, for three teeth used in time domain simulation. The peak-to-peak variation is approximately 0.48 mm.

The time domain simulation has three special requirements for the selected tool: use the actual tooth angles, include the radius variation as runout, and incorporate the bull nose geometry. For the tooth angles, the measured angles from the scanned edge were arranged in an array, where the columns were the individual teeth and the rows were the z locations (in steps of 0.1 mm). These z locations extended over the entire cutting length, but the array was truncated to include rows only up to the commanded axial depth when the simulation was executed. This enables any axial depth to be simulated (up to the cutting length). A row array of closely spaced tooth angles for use in the time domain simulation was then defined. The resolution in this array was: $\Delta\phi = 360/SR$, where SR is the number of steps per revolution in the simulation.

Once this array was defined, the measured tooth angles were specified in an index array with each entry given by: `round`($\phi/\Delta\phi$), where ϕ is the measured angle of the tooth at the selected z location and `round` is the MATLAB function that rounds to the nearest integer value. This index array was then used to specify the angle of any tooth at any z location by identifying the nearest preselected value from the closely spaced tooth angle array for use in the simulation. The reason for this approach is that the current chip thickness in milling depends not only on the commanded chip thickness and current vibration, but also the surface left by the previous teeth at the current tooth angle. To be able to do so conveniently, this information must be organized according to specified tooth angles.

The tool's radius variation was included as runout, as noted. The z-dependent RO values for each tooth were also arranged in an array, where the columns were the individual teeth and the rows were the z locations (again in steps of 0.1 mm). Note that the RO values are negative in Fig. 11. A negative RO value reduces the chip thickness for the current tooth, but leaves behind material that the next tooth must remove (and therefore increases that chip thickness).

Two other data organization requirements were: 1) the surface that was left behind by the current tooth; and 2) the actual commanded chip thickness. To keep track of the previously machined surface, another array was defined that recorded the surface location in the tool's normal direction for each simulation time step. The columns of this matrix were the number of steps per revolution and the rows were the z locations. The influence of runout on subsequent chip thickness values was captured in this matrix.

Because there were small variations in the tooth angles from the nominal helix profile (Fig. 7), the commanded chip thickness was also modified to account for the actual tooth angle using the circular tooth path approximation. This approximation calculates the nominal chip thickness from the product of the feed per tooth and the sine of the tooth angle. Finally, the bull nose portion of the endmill was incorporated in the simulation by projecting the forces in the appropriate directions using the nose surface normal at each z location. Also, the axial depth was updated to account for the arc length on the nose radius [1].

Given this information, the simulation proceeded as follows:

1. The instantaneous chip thickness, $h(t)$, was determined using the commanded chip thickness, runout, and vibration of the current and previous teeth at the selected tooth angle.
2. The cutting force components in the tangential, t, and normal, n, directions were calculated at each axial slice using:

$$F_t(t) = k_{tc} b h(t) + k_{te} b \quad (1)$$

$$F_n(t) = k_{nc} b h(t) + k_{ne} b \quad (2)$$

where b is the slice width (0.1 mm) and the cutting force coefficients are identified by the subscripts: t or n for

direction; and *c* or *e* for cutting or edge effect. These forces were then summed over all axial slices engaged in the cut.

3. The summed force components were used to find the new displacements by numerical solution of the differential equations of motion in the *x* (feed) and *y* directions:

$$m_x\ddot{x} + c_x\dot{x} + k_x x = F_t(t)\cos\phi + F_n(t)\sin\phi \quad (3)$$

$$m_y\ddot{y} + c_y\dot{y} + k_y y = F_t(t)\sin\phi - F_n(t)\cos\phi \quad (4)$$

where *m* is the modal mass, *c* is the modal viscous damping coefficient, and *k* is the modal stiffness. The subscripts identify the direction and multiple degrees-of-freedom in each direction can be accommodated.

4. The tool rotation angle was incremented by adding one to each entry in the tooth angle index array and the process was repeated.

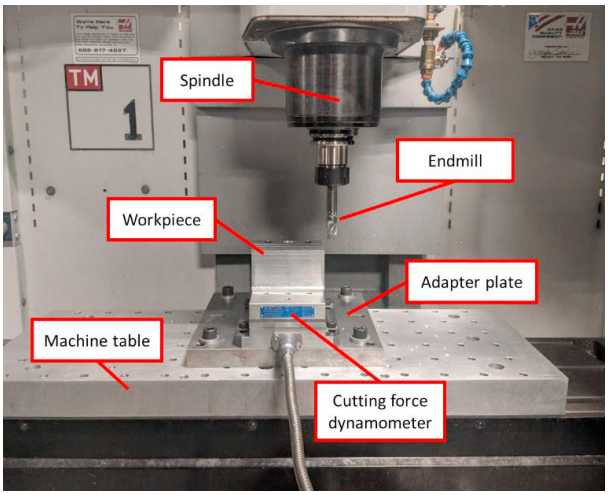

Fig. 12. Experimental setup for milling force measurement.

4. Experimental setup

The experimental setup for milling force measurement is shown in Fig. 12. Trials were completed on a Haas TM-1 three-axis computer numerically controlled (CNC) milling machine. The 7075 aluminum workpiece was mounted on a cutting force dynamometer (Kistler 9257B) and the endmill was clamped in a collet holder and inserted in the CAT-40 spindle interface. Tests were performed at axial depths of cut from 4 mm to 14 mm. The commanded feed per tooth for these down (climb) milling experiments was 75 µm/tooth, the spindle speed was 4000 rpm, and the radial depth of cut was 2 mm (12.5% radial immersion). In a second set of tests, the axial depth was held constant at 8 mm and the feed per tooth was varied from 25 µm/tooth to 125 µm/tooth. The same spindle speed and radial depth were used. The tool and workpiece frequency response functions, or FRFs, were measured by impact testing, where an instrumented hammer is used to excite the structure and the response is measured using a linear transducer (a low-mass accelerometer for this research). The results are presented in Fig. 13. Modal fitting was applied to extract the modal parameters for the time domain simulation; see Table 1.

Table 1. Modal parameters for force measurement setup.

Tool			
Direction	*m* (kg)	*k* (N/m)	*c* (N-s/m)
x	0.756	2.50×10^7	522
x	0.257	1.25×10^7	179
x	0.381	4.95×10^7	348
x	0.120	1.85×10^7	75
x	0.209	6.00×10^7	283
y	0.294	1.07×10^7	105
y	1.101	6.65×10^7	106
y	0.392	4.25×10^7	684
y	27.774	4.00×10^7	162
y	0.140	2.27×10^7	2666
y	0.118	3.33×10^7	142
Workpiece			
Direction	*m* (kg)	*k* (N/m)	*c* (N-s/m)
x	0.373	3.37×10^7	496
x	1.039	1.10×10^8	363
x	0.466	6.00×10^7	180
x	0.019	1.12×10^7	232
y	95.576	1.67×10^8	10612
y	73.651	1.77×10^9	12276
y	21.054	2.03×10^9	7856
y	2.780	4.32×10^8	3258
y	3.203	7.67×10^8	1983
y	1.616	5.87×10^8	2279

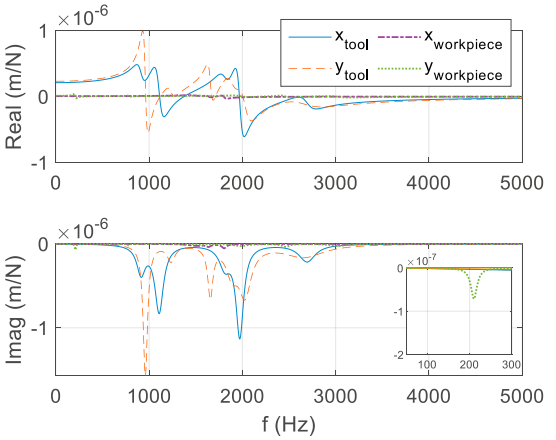

Fig. 13. FRFs of tool and workpiece for force measurement setup.

The setup for stability testing was similar to Fig. 12, but the aluminum workpiece was mounted on a parallelogram, leaf-type flexure rather than the dynamometer (the flexible direction for the flexure was oriented parallel with the machine's *x* direction); see Fig. 14. The modal parameters are listed in Table 2; note that the workpiece (flexure) *x* direction is significantly more flexible than the tool.

Table 2. Modal parameters for stability testing setup.

Tool			
Direction	m (kg)	k (N/m)	c (N-s/m)
x	0.593	2.01×10^7	416
x	0.328	1.50×10^7	222
x	0.095	1.44×10^7	94
x	0.124	3.50×10^7	333
y	0.325	1.20×10^7	119
y	0.784	5.00×10^7	889
y	0.550	6.00×10^7	228
y	0.338	5.00×10^7	247
y	0.210	3.50×10^7	130
y	0.176	5.10×10^7	394
Workpiece			
Direction	m (kg)	k (N/m)	c (N-s/m)
x	2.976	1.74×10^6	93
y	79.056	2.50×10^7	1067
y	52.482	1.12×10^8	13800
y	214.842	1.32×10^9	21301
y	17.026	2.44×10^8	5285
y	2.958	7.07×10^7	1215

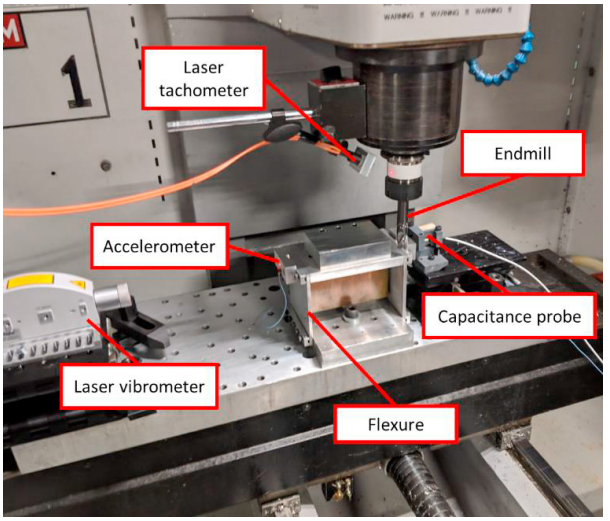

Fig. 14. Experimental setup for stability testing.

The cutting force coefficients for the 7075 aluminum workpiece were: k_{tc} = 1150 N/mm^2, k_{nc} = 522 N/mm^2, k_{te} = 25 N/mm, and k_{ne} = 25 N/mm. The same values were used for all predictions.

5. Results

Measured and predicted feed direction force values, F_x, for b = {4, 6, 8, 12, and 14} mm are shown in Figs. 15-19. Good agreement is observed in all cases, although the dynamometer dynamics add oscillations to the measured force. It is also seen that the force progresses from a smooth profile while engaged in the cut for b = 4 mm to highly discontinuous at b = 14 mm. This is the result of the tool design which cuts with "bands" of limited axial depth, where this depth is defined by the spatial period of the radius variation along the tooth helix (Fig. 6). As the axial depth increases, more bands are individually engaged and the force is subsequently increasingly discontinuous.

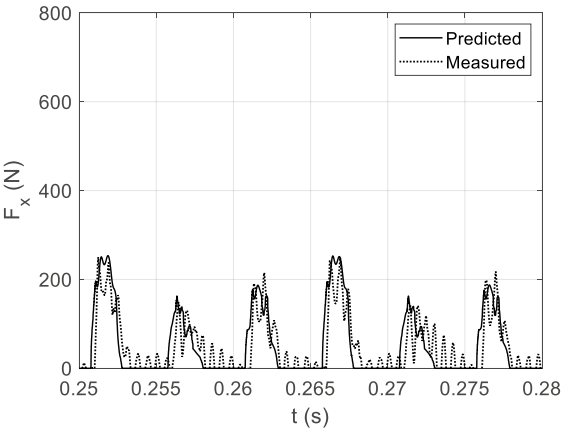

Fig. 15. Measured and predicted force for b = 4 mm.

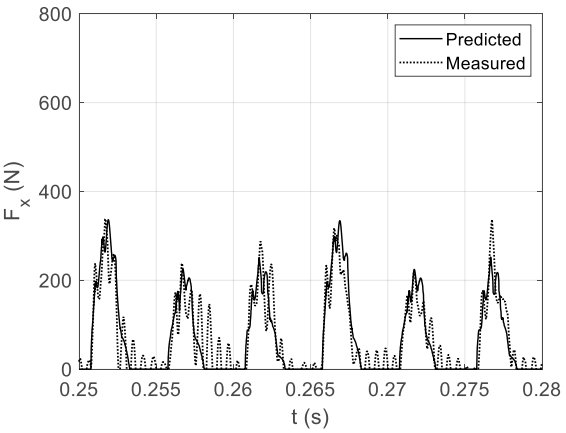

Fig. 16. Measured and predicted force for b = 6 mm.

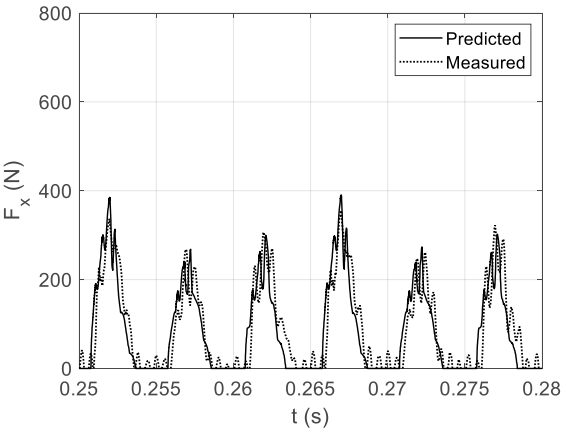

Fig. 17. Measured and predicted force for b = 8 mm.

Figures 20-24 display measured and predicted F_x results for feed per tooth values of {25, 50, 75, 100, and 125} µm/tooth. While the force levels grow with the increased chip thickness,

they do not become significantly more discontinuous. This is because the axial depth was fixed at 8 mm for these tests.

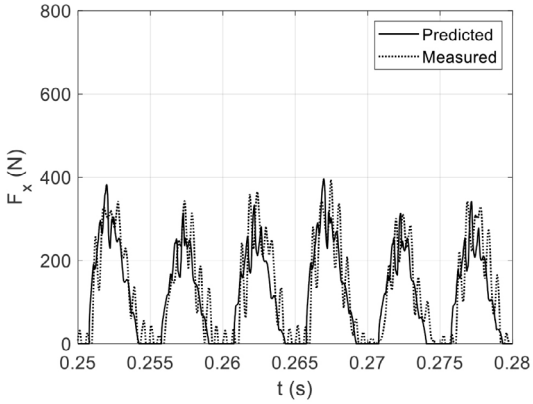

Fig. 18. Measured and predicted force for b = 12 mm.

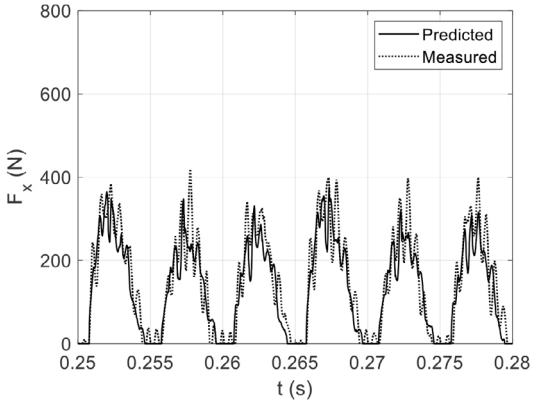

Fig. 19. Measured and predicted force for b = 14 mm.

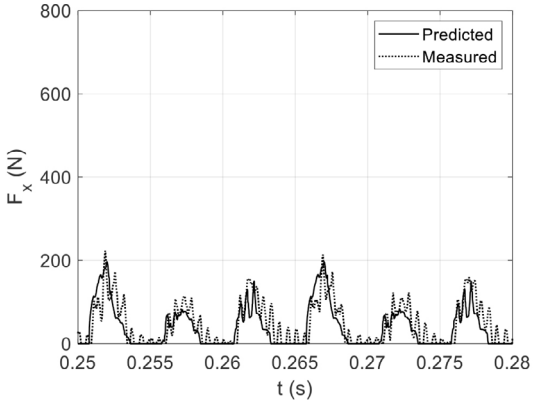

Fig. 20. Measured and predicted force for f_t = 25 µm/tooth.

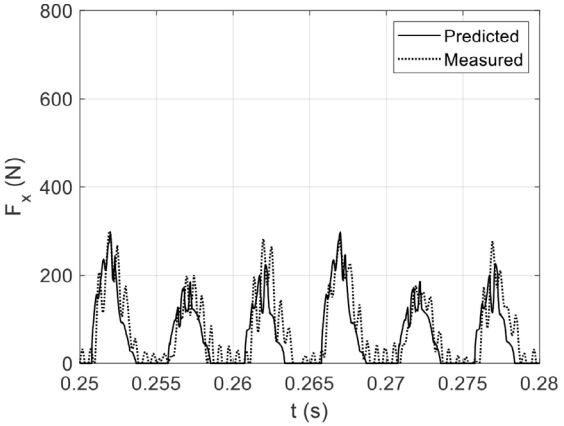

Fig. 21. Measured and predicted force for f_t = 50 µm/tooth.

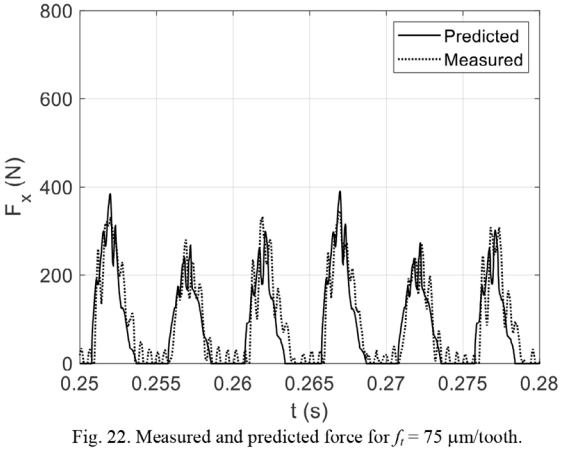

Fig. 22. Measured and predicted force for f_t = 75 µm/tooth.

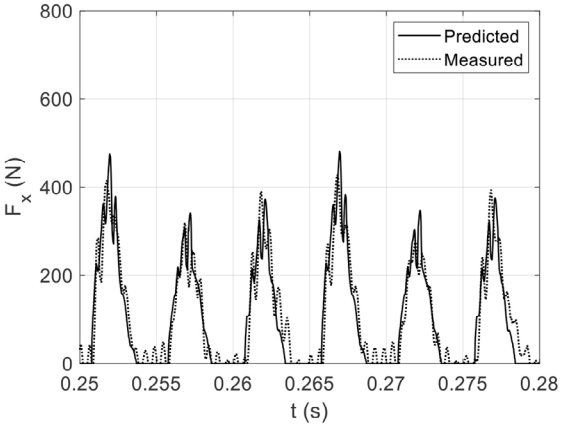

Fig. 23. Measured and predicted force for f_t = 100 µm/tooth.

Given the validated force results, stability testing was completed using the Fig. 14 setup. Workpiece (flexure) displacement and velocity predictions were generated using the time domain simulation, where the system dynamics were defined by Table 2. The down milling radial depth of cut was 3 mm and the commanded feed per tooth was 100 µm/tooth.

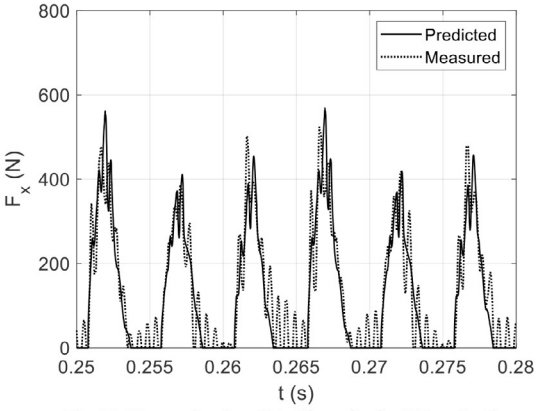

Fig. 24. Measured and predicted force for f_t = 125 µm/tooth.

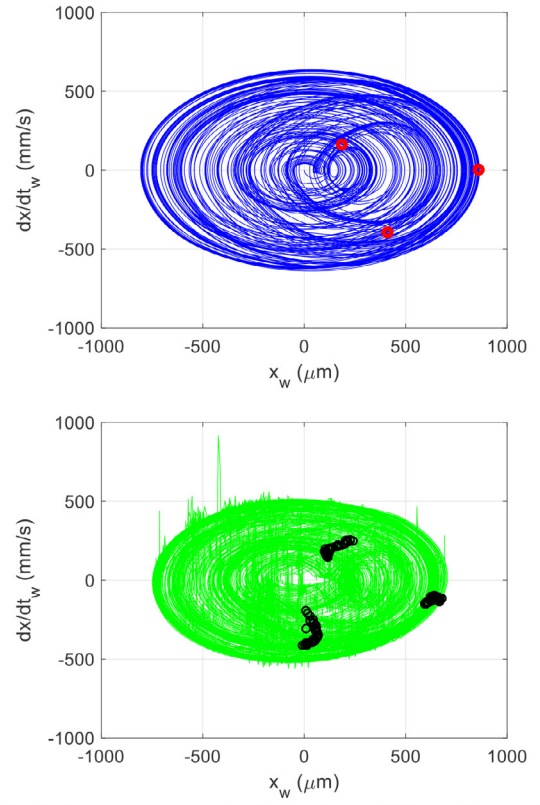

Fig. 25. Poincaré maps for period-3 bifurcation at {2750 rpm, 10 mm}. (Top) predicted. (Bottom) measured.

To establish stability, the workpiece x direction displacement and velocity signals were sampled once per revolution (i.e., at the spindle rotating frequency) [13-14]. This periodic sampling approach was used to determine if the milling response was synchronous with the spindle rotation or not by constructing Poincaré maps (i.e., the periodically sampled displacement versus the periodically sampled velocity) for both experiment and prediction. To interpret these Poincaré maps, if the cut is stable (i.e., it exhibits forced vibration only), the data repeats with each spindle revolution and the sampled points appear at one location. If self-excited vibration (i.e., chatter, or secondary Hopf bifurcation) occurs, however, an elliptical distribution of sampled points is observed due to the presence of both the (generally) incommensurate chatter frequency and the tooth passing frequency (and its harmonics). Additionally, period-n bifurcations can occur, where n represents the number of periods between repetition. A period-3 bifurcation, for example, exhibits motion that repeats every three rotations. Results are presented in Figs. 25-30 for multiple spindle speed-axial depth combinations, where the once-per-revolution samples (circles) are superimposed on the continuous x direction workpiece displacement, x_w, and velocity, dx/dt_w. Good agreement is observed in each case.

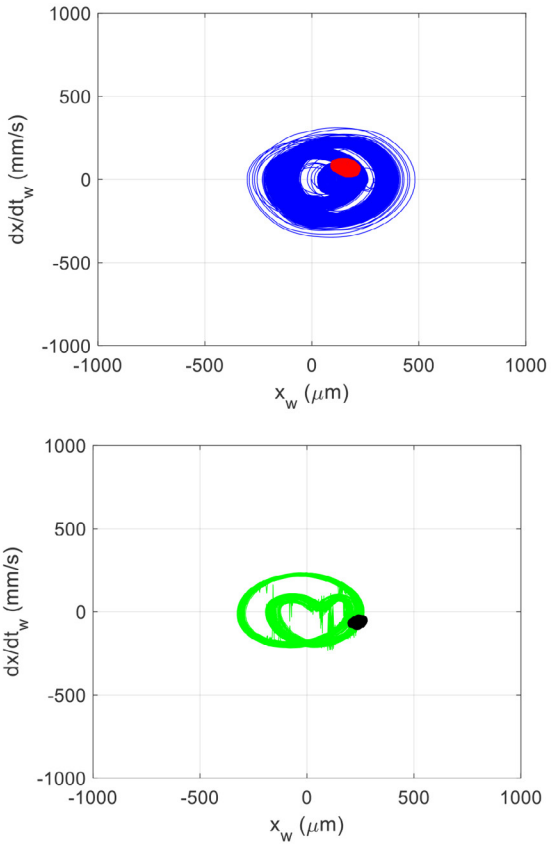

Fig. 26. Poincaré maps for marginally stable cutting at {3300 rpm, 10 mm}. (Top) predicted. (Bottom) measured.

6. Conclusions

This paper provides a reverse engineering solution for modeling the behavior of non-standard edge geometry endmills. Structured light scanning was used to produce a solid model of the endmill. From this model, spatial coordinates for the points that define the cutting edges were extracted. The points were then used to determine the cutting edge radius and angle at equally spaced points along the tool axis. The cutting edge geometry was then incorporated in a time domain simulation that was used to predict cutting force and deflection. Good agreement between predicted and measured cutting forces was obtained.

The simulation was then applied to predict stability using a period sampling strategy. Poincaré maps were produced using both the predicted and experimental displacement and velocity signals. Marginally stable, secondary Hopf bifurcation, and period-3 bifurcation results were obtained. Again, good agreement between prediction and measurement was observed. Industrial application of this approach will enable: 1) selection of stable machining parameters for non-standard edge geometry endmills at the process planning stage; 2) prediction of force and deflection levels for these optimum parameters; and 3) evaluation of the relationship between tool wear, force, and stability by monitoring changes in the edge geometry by repeated scans during interrupted machining trials.

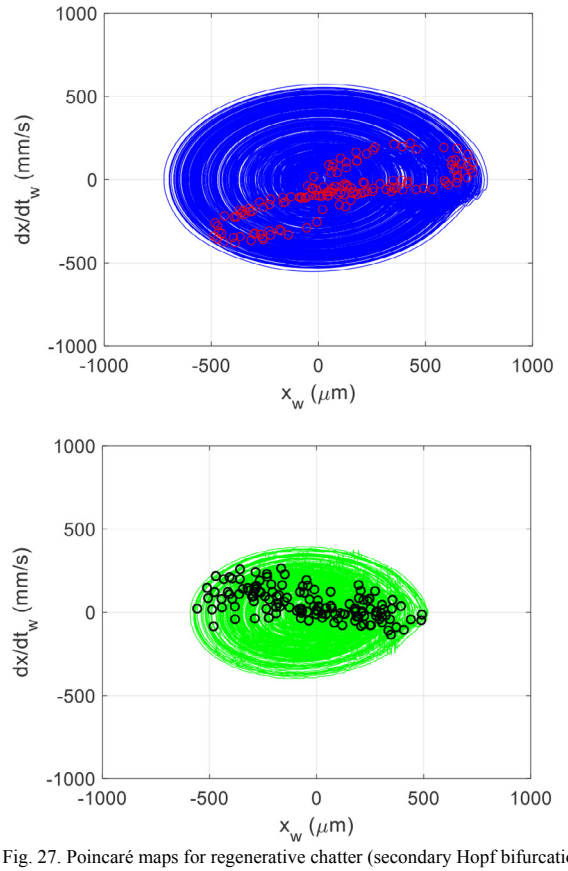

Fig. 27. Poincaré maps for regenerative chatter (secondary Hopf bifurcation) at {4000 rpm, 10 mm}. (Top) predicted. (Bottom) measured.

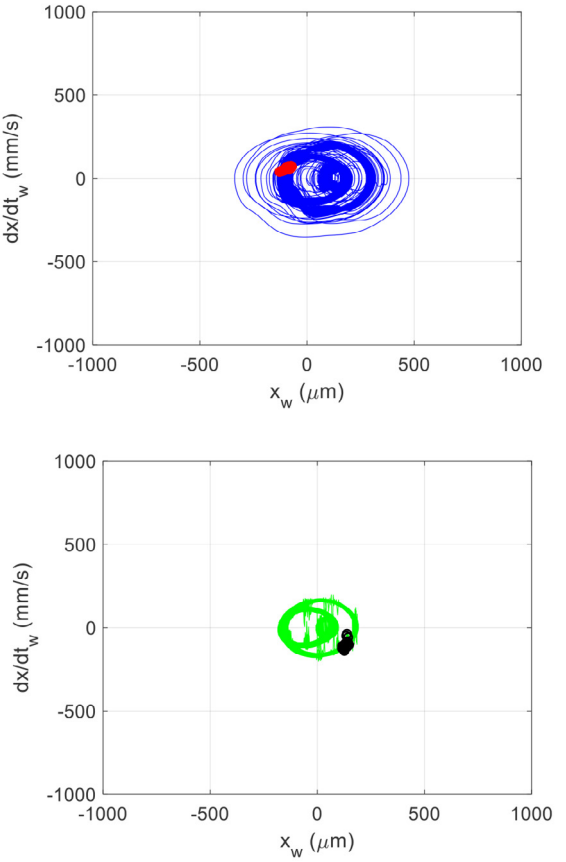

Fig. 28. Poincaré maps for marginally stable cutting at {3380 rpm, 10 mm}. (Top) predicted. (Bottom) measured.

Acknowledgements

The authors gratefully acknowledge financial support from MAI BA-21 (USAF contract number FA8650-17-2-5246).

References

[1] Schmitz, T.L. and Smith, K.S., 2009, Machining Dynamics: Frequency Response to Improved Productivity, Springer, New York, NY.
[2] Altintas, Y., 2012, Manufacturing Automation: Metal Cutting Mechanics, Machine Tool Vibrations, and CNC Design, Cambridge University Press.
[3] Altintas, Y. and Weck, M., 2004, Chatter stability of metal cutting and grinding, CIRP Annals-Manufacturing Technology, 53/2: 619-642.
[4] Wang, J.-J. and Yang, C.S., 2003, Angle and frequency force models for a roughing end mill with a sinusoidal edge profile, International Journal of Machine Tools and Manufacture, 43: 1509-1520.
[5] Merdol, S.D. and Altintas, Y., 2004, Mechanics and Dynamics of Serrated Cylindrical and Tapered End Mills, Journal of manufacturing Science and Engineering, 126: 317-326.
[6] Dombovari, Z., Altintas, Y., and Stepan, G., 2010, The effect of serration on mechanics and stability of milling cutters, International Journal of Machine Tools and Manufacture, 50: 511-520.
[7] Dombovari, Z., Munoa, J., and Stepan, G., 2012, General milling stability model for cylindrical tools, Procedia CIRP, 4: 90-97.

[8] Stepan, G., Munoa, J., Insperger, T., Surico, M., Bachrathy, D., and Dombovari, Z., 2014, Cylindrical milling tools: Comparative real case study for process stability, CIRP Annals-Manufacturing Technology, 63: 385-388.
[9] Koca, R., and Budak, E., 2013, Optimization of serrated mills for reduced cutting energy and higher stability, Procedia CIRP, 8: 570-575.
[10] Grabowski, R., Denkena, B., and Köhler, J., 2014, Prediction of process forces and stability of end mills with complex geometries, Procedia CIRP, 14: 119-124.
[11] Tehranizadeh, F., and Budak, E., 2017, Design of serrated end mills for improved productivity, Procedia CIRP, 58: 493-498.
[12] Smith, K.S. and Tlusty, J., 1991, An overview of modeling and simulation of the milling process, ASME Journal of Engineering for Industry, 113/2: 169-175.
[13] Honeycutt, A. and Schmitz, T., 2016, A mew metric for automated stability identification in time domain milling simulation, Journal of Manufacturing Science and Engineering, 138/7: 074501.
[14] Honeycutt, A. and Schmitz, T., 2017, Milling stability interrogation by subharmonic sampling, Journal of Manufacturing Science and Engineering, 139/4: 041009.

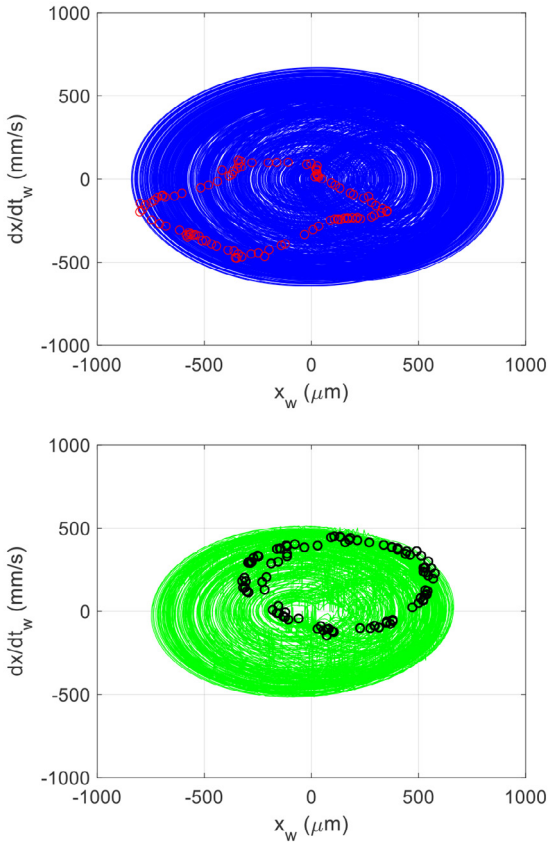

Fig. 29. Poincaré maps for regenerative chatter (secondary Hopf bifurfaction) at {2850 rpm, 10 mm}. (Top) predicted. (Bottom) measured.

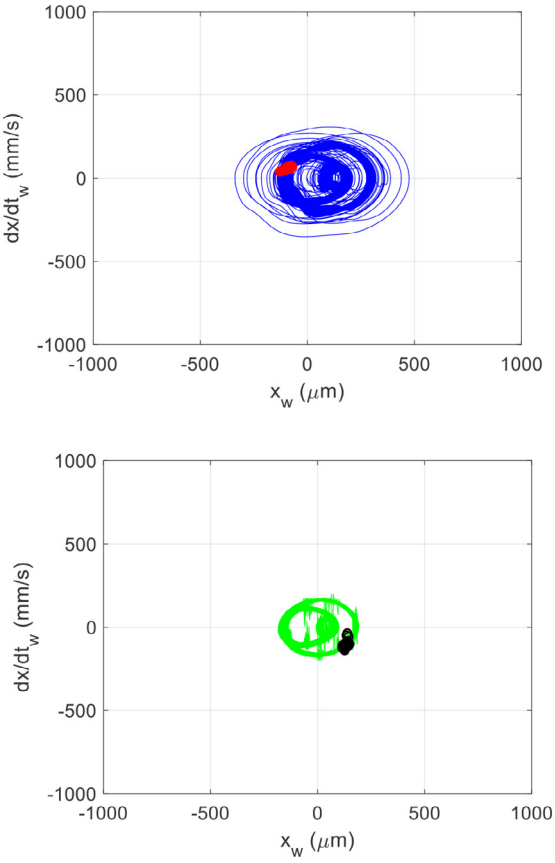

Fig. 30. Poincaré maps for marginally stable cutting at {3400 rpm, 10 mm}. (Top) predicted. (Bottom) measured.